NJC

PAPER

View Article Online
View Journal | View Issue

Cite this: *New J. Chem.*, 2016, **40**, 4678

A novel gas sensor based on porous α-Ni(OH)$_2$ ultrathin nanosheet/reduced graphene oxide composites for room temperature detection of NO$_x$†

Ying Yang,[ab] Hongjie Wang,[a] Linlin Wang,[a] Yunlong Ge,[a] Kan Kan,[a] Keying Shi*[a] and Junhong Chen*[c]

Received (in Montpellier, France) 20th November 2015,
Accepted 10th March 2016

DOI: 10.1039/c5nj03284a

www.rsc.org/njc

A novel composite room temperature (RT) gas sensor based on a α-Ni(OH)$_2$ thin nanosheet (TNS)/reduced graphene oxide composite (α-Ni(OH)$_2$ TNS/rGO composites) was successfully synthesized *via* a facile reflux method. In this synthesis, Ni^{2+} and urea were adsorbed on GO through electrostatic interactions in a water solution. The subsequent reflux treatment led to the transformation of the Ni(OH)$_2$ TNS coated on GO and also to the reduction of graphene oxide. Compared to the pristine Ni(OH)$_2$ TNS prepared in the absence of GO, the prepared α-Ni(OH)$_2$ TNS/rGO composite showed higher NO$_x$ gas sensing performance with a low detection limit of 970 ppb, high response and fast response at RT. The enhanced sensing properties are attributed to the synergy of the superior conductivity of rGO and the 3D nanostructure of the α-Ni(OH)$_2$ TNS/rGO composite. The present strategy for combining various hydroxide and nanoscaled building blocks into integrated 3D structures will open new opportunities for designing and synthesizing multifunctional composites.

Introduction

Metal oxides like ZnO,[1–3] In_2O_3,[4–6] SnO_2,[7–9] CuO[10,11] *etc.* used as sensor materials have attracted much scientific attention due to their high response and fast response to hazardous gases. The detection of NO$_x$ gas, which is one of the most noxious, poisonous and abundant air pollutants, is of great importance from the viewpoint of both environmental protection and human health. The NO$_x$ sensors with excellent performance and their composites have been reported in the literature.[12–15] Unfortunately, most of these devices are operated at higher temperatures and the further development of sensors was restricted. Therefore, many efforts are currently being made to develop sensors that can effectively detect NO$_x$ at RT. In our previous work,[16] the gas-sensing performance of the α-Ni(OH)$_2$ thin-film sensor to NO$_x$ was studied and the results were satisfactory. However, there is the potential that the response and response time of the α-Ni(OH)$_2$ thin-film sensor can be improved, compared with the sensors operated under high temperature. The Ni(OH)$_2$/carbon black composite thin-film sensor was synthesized to detected NO$_x$ gas and the operating temperature for the composites can down to room temperature.[17] Therefore, the introduction of an appropriate substrate for the composite can effectively improve the response of the sensing materials.

Graphene (GN), which was first isolated from bulk graphite in 2004, has become a sparkling rising star on the horizon of materials science in the last several years. It possesses fascinating electronic, chemical and mechanical properties, such as high intrinsic electrical conductivity, a large surface area, chemical stability, excellent flexibility and stiffness. The unique structure and outstanding properties make GN an ideal building block for intercalated composites. Intercalated composites are multiphase materials obtained through the dispersion of an organic or inorganic phase into the matrix, resulting in a combination and synergistic effect of the individual properties of the component materials. In recent years, research on intercalated composites has been very active, especially in the field of catalysis, electrode materials, sensors and charge storage. A large number of intercalation composites with graphene as the matrix have been successful synthesized, such as TiO_2,[18–20] SnO_2,[21–23] CuO,[24,25] and Fe_3O_4,[26–28] and the photocatalysis, electrochemistry,

[a] *Key Laboratory of Functional Inorganic Material Chemistry, Ministry of Education, Key Laboratory of Physical Chemistry, School of Chemistry and Material Science, Heilongjiang University, Harbin, 150080, P. R. China. E-mail: shikeying2008@163.com; Fax: +86 4518667 3647; Tel: +86 451 8660 9141*
[b] *Key Laboratory of Applied Chemistry and Nanotechnology at Universities of Jilin Province, Changchun University of Science and Technology, Changchun 130022, P. R. China*
[c] *Department of Mechanical Engineering, University of Wisconsin-Milwaukee, 3200 North Cramer Street, Milwaukee, Wisconsin 53211, USA*

† Electronic supplementary information (ESI) available: A TEM image of GO, elemental mapping of C2, the XRD pattern of GO and rGO, SEM of the pure α-Ni(OH)$_2$, bar graphs for gas selectivity, data of response and response time, fitted impedance parameters of samples. See DOI: 10.1039/c5nj03284a

magnetic and photoelectric conversion properties of the materials were improved effectively. In 2010, Dai *et al.*[29,30] reported that the nickel hydroxide/graphene composite showed high electrochemical performance. In 2015, Na *et al.*[31] reported improved sensing behaviors in reduced graphene oxide functionalized with $Ni(OH)_2$ nanoparticles towards NO_2. The Cu_xO/graphene-composite was synthesized by using graphene as a substrate for NO_x gas sensing applications in our previous work.[32] Therefore, graphene is an excellent substrate for constructing a metal oxide/graphene composite with enhanced sensing properties. In this paper, the intercalation nanocomposite of partially reduced graphene oxide (rGO) supported α-$Ni(OH)_2$ was studied systematically and applied to the gas-sensor field for the first time. Chen *et al.* reported[33,34] that the rGO exhibits good gas-sensing performance to NO_x at RT; however, the response speed and the recovery process need to be improved. By combination with α-$Ni(OH)_2$, we synthesized a material with enhanced gas-sensing performance, including improved response, response time and desorption.

Hence, the porous α-$Ni(OH)_2$ thin nanosheet (TNS)/reduced graphene oxide composite (α-$Ni(OH)_2$ TNS/rGO composites) was successfully prepared *via* a two-step method, as shown in Scheme 1. First, owing to the oxygen-containing functional groups on the GO (such as carbonyl, epoxy groups and hydroxyl), the surface of GO is electronegative and interacts strongly with coated species. A mass of Ni^{2+} ions were absorbed onto the GO under ultrasonic conditions. By using urea as the precipitant, tiny α-$Ni(OH)_2$ nanoparticles were uniformly coated on the GO by hydrolysis of $Ni(NO_3)_2$. Second, the newly generated α-$Ni(OH)_2$ nanoparticles recrystallized and assembled into the porous α-$Ni(OH)_2$ ultrathin nanosheets accompanied by peeling to thinner layers of graphene. The growth process and the formation mechanism of the α-$Ni(OH)_2$ TNS/rGO nanocomposite and its gas-sensing mechanism for NO_x were also analyzed. The α-$Ni(OH)_2$ TNS/rGO nanocomposite presents better gas-sensing performance than α-$Ni(OH)_2$. Owing to the synergistic effect of α-$Ni(OH)_2$ and rGO, not only was the response of α-$Ni(OH)_2$ enhanced greatly (79.9%) and response time reduced on the whole, but also the problem of recovering rGO was overcome. The approach of growing α-$Ni(OH)_2$ nanoparticles on GO could be applied to other metal oxides and should be very helpful for developing more effective gas sensors.

Experimental

Synthesis of α-$Ni(OH)_2$/reduced graphene oxide composites

GO was synthesized from natural graphite using a modified Hummers method, as described in the literature. Other analytical grade chemicals were purchased and used without further purification. For a typical preparation of the α-$Ni(OH)_2$ TNS/RGO composite, $Ni(NO_3)_2{\cdot}6H_2O$ and GO were dispersed in water in accordance with a certain proportion of mass, giving a dispersion by ultrasonication.

By adding a certain amount of urea into the above suspension, which was then reflux distilled for 3 h at 100 °C under magnetic stirring, the black precipitate was obtained. The product was then washed by deionized water several times after cooling to RT. Finally, the product was dried at 60 °C for 24 h in an oven to produce a black powder. The obtained composites were synthesized by the reflux of 0.016 mol L^{-1} $Ni(NO_3)_2{\cdot}2H_2O$. The mass ratios of $Ni(NO_3)_2{\cdot}6H_2O$ and GO are 5 : 1, 10 : 1, 15 : 1 and 25 : 1, and the composites were named as C1, C2, C3 and C4, respectively. Meanwhile as control experiments the pure α-$Ni(OH)_2$ without GO and rGO was synthesized under the same conditions.

Material characterization

The structures and compositions of the as-prepared products were characterized by XRD (D/max-IIIB-40 KV, Japan, Cu-Kα radiation, λ = 1.5406 Å) and FTIR spectra (Perkin Elmer Spectrometer, KBr pellet technique). The morphologies of the synthesized samples were studied by SEM (Philips XL-30-ESEM-FEG, 5–20 kV) and transmission electron microscopy (TEM, JEOL-JEM-2100, 200 Kv). Thermal analysis employed a TG/DTA instrument (TA-SDTQ600, heating rate: 10 °C min^{-1} in air).

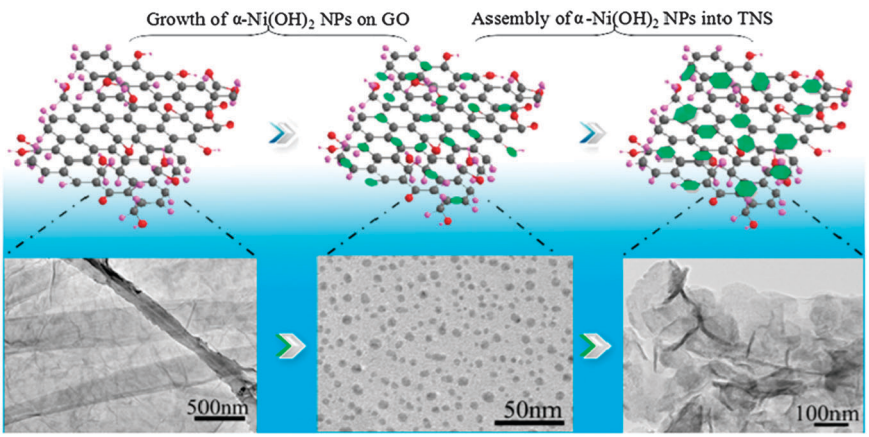

Scheme 1 Illustration of the fabrication process of α-$Ni(OH)_2$ TNS/rGO nanocomposites. Dark gray balls represent C atoms; pink balls, H atoms; red balls, O atoms; green nanoparticles and nanosheets, α-$Ni(OH)_2$.

The Brunauer–Emmett–Teller (BET) surface area of the products was measured by using N_2 adsorption–desorption (TriStar II 3020); the sample was dried for 10 h at 150 °C under vacuum before the measurement. The quantitative analysis of elements was conducted using an elemental analysis (EA) instrument (Elemental, vario Micro). Electrochemical impedance spectroscopy (EIS) and Mott-Schottky (MS) plot measurements were carried out by using an electrochemical working station (CHI660C, Shanghai, China) in a half-cell setup configuration at RT. In the EIS measurement, the range of frequency was 0.01 Hz–100 kHz and the excitation amplitude was 5 mV.

Gas sensing tests

An interdigitated Au electrode (7 × 5 × 0.38 mm) was selected for gas sensing detection and the electrode spacing was 20 μm. A certain amount of α-$Ni(OH)_2$ was dispersed in ethanol to form a suspension, then the suspension was spin-coated onto the interdigitated electrode to form a sensitive film and dried at 70 °C for 5 h to obtain a thin film gas sensor. The sensor was installed into a test chamber with an inlet and an outlet. The chamber was flushed with air for 2 min to remove any contaminants from the flask and also to stabilize the film before testing. A syringe was used to inject the required volume of NO vapor into the chamber. The changes in the electrical resistance of the sample over time were recorded by a home-made automatic resistance apparatus, and the chamber was purged with air to recover the sensor resistance. The sensor response was defined as the ratio $(R_N - R_0)/R_0$, where R_0 is the sensor resistance in air, and R_N is the resistance in NO_x gas. The response time is defined as the time required for the variation in resistance to reach 85% of the equilibrium value after a test gas was injected. The test was conducted at room temperature (20 °C) with a relative humidity (RH) of around 40%.

Results and discussion

Composition and morphology

The morphology and structure of the prepared GO were investigated by TEM as shown in Fig. S1 (ESI†). The GO synthesized using a modified Hummers method is thin and transparent, and it is an ideal substrate for building up a 3D nanostructure. The porous α-$Ni(OH)_2$ TNS/rGO composites were successfully prepared by reflux for 3 h at 100 °C. The typical sample α-$Ni(OH)_2$ TNS/rGO composite (C2, with a mass ratio of $Ni(NO_3)_2{\cdot}6H_2O$ and GO was 10 : 1) was investigated by SEM and TEM as shown in Fig. 1. The representative SEM and TEM images of C2 in Fig. 1a and b demonstrate that the 3D nanoflower-like α-$Ni(OH)_2$ was evenly and uniformly loaded on the rGO surface. The low magnification TEM image of α-$Ni(OH)_2$ in Fig. 1c displays the hierarchical flower-like microstructures that consist of porous thin nanosheets. In Fig. 1d, the ten-layer edge of rGO can be seen in the C2. The HR-TEM image of C2 is displayed in Fig. 1f. The fringe spacing is about 0.27, and 0.38 nm, corresponding to the (101) and (006) crystal planes of the hexagonal α-$Ni(OH)_2$. The average diameter of

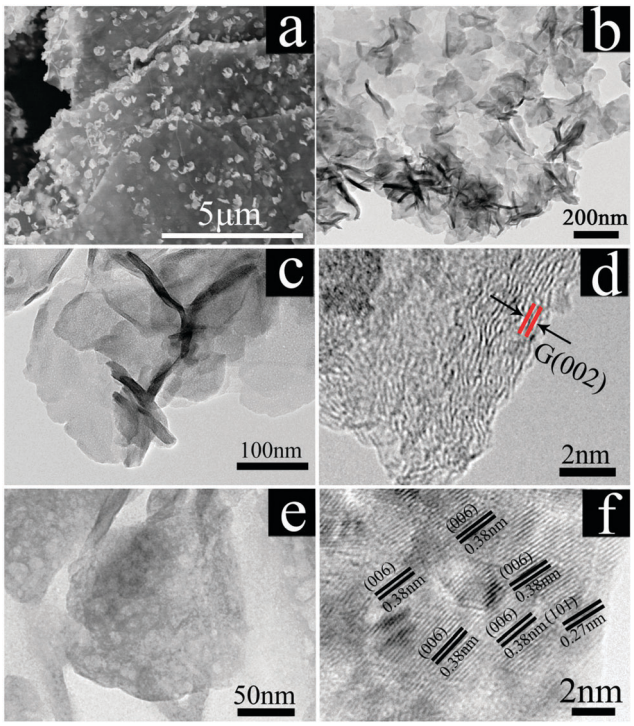

Fig. 1 (a) SEM image of the synthesized α-$Ni(OH)_2$ TNS/rGO composite (C2); (b) TEM image of the C2; (c) representative TEM image of C2; (d) TEM image of part of the composite with more than 10 graphitic layers; (e) TEM image of the α-$Ni(OH)_2$ on the composite; (f) HRTEM image of C2, in which the (101), (018), and (006) of $Ni(OH)_2$ can be seen.

α-$Ni(OH)_2$ is about 2–3 nm. These hierarchical microstructures with many pores on α-$Ni(OH)_2$ act as gas adsorption, dispersion and desorption channels, eventually resulting in enhanced gas sensing.

In order to determine the spatial distribution of the elements through the whole composite (C2), elemental mapping was carried out, as shown in Fig. S2 (ESI†). Fig. S2a (ESI†) is a bright field image of the C2. Fig. S2(b)–(d) (ESI†) reveal the existing C, Ni, and O elements. These images clearly show that the distribution of the Ni, O and C elements is uniform throughout the whole C2 sample.

The obtained products have been confirmed by X-ray powder diffraction (XRD). As control samples, Fig. 2A shows the XRD pattern of the partially reduced graphene oxide (rGO) on GO without $Ni(NO_3)_2{\cdot}6H_2O$. The weak diffraction peak at $2\theta = 12.2°$ can be indexed to the (001) plane of graphite oxide, and the broad diffraction peak at 2θ of 24.5–27.5° can be indexed to the (002) planes of graphite (G).[35] Compared with the XRD patterns of graphite oxide (seen in Fig. S3, ESI†) made using a modified Hummers method, the (001) peak of graphite oxide was greatly reduced, and the very broad (002) peak of graphite can be seen, suggesting that the graphite component is very poorly ordered along the stacking direction. This is an indication that the sample is composed of exfoliated graphene sheets. In addition, the shift of the (001) plane from $2\theta = 10.6$ to $2\theta = 12.2°$ indicates that the layer spacing decrease owing to the functional groups (–COOH, –OH) on the edge of GO was reduced. This signifies

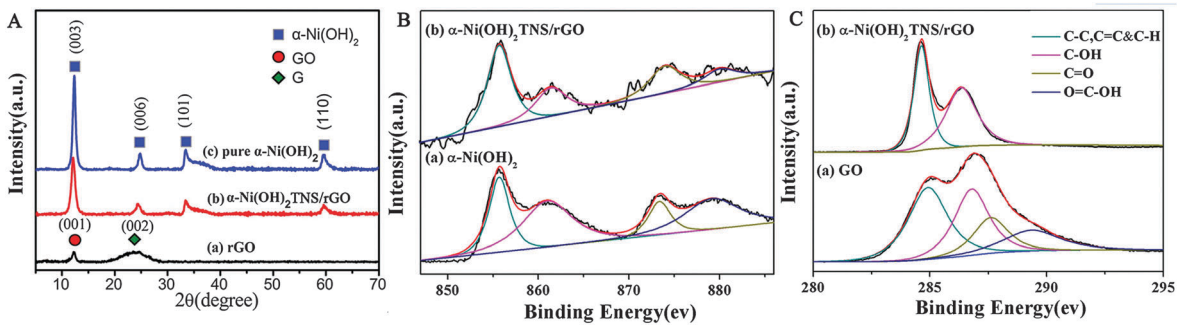

Fig. 2 XRD patterns of the synthesized samples (A): (a) rGO; (b) the α-$Ni(OH)_2$ TNS/rGO composite (C2); (c) the pure α-$Ni(OH)_2$ and XPS spectra of the synthesized samples; (B) Ni 2p; (C) O 1s.

that the as-prepared graphite oxide indeed became partially reduced graphene oxide (rGO) by reflux. In Fig. 2A(b), all diffraction peaks can be ascribed to the (003), (006), (101) and (110) planes of α-$Ni(OH)_2$ with a hexagonal structure in the α-$Ni(OH)_2$ TNS/RGO composite.[36–38] The missing diffraction peaks of the (001) planes (GO) and the (002) planes (G) may be due to both the partial reduction of the GO and the coverage effect of strong diffraction peaks of α-$Ni(OH)_2$. Moreover, all of the peaks of α-$Ni(OH)_2$ on the rGO are weaker than those of the pure α-$Ni(OH)_2$ (Fig. 2A(c)), which may be caused by morphological changes to the α-$Ni(OH)_2$ in the composite; the former SEM and TEM results verify this assumption.

To determine the chemical composition of porous α-$Ni(OH)_2$ TNS/rGO composites, X-ray photoelectron spectroscopy (XPS) measurements were carried out in the region of 0–1300 eV (Fig. 2B and C). Moreover, XPS can reveal the interaction between different components that directly affects the performance of a composite. Fig. 2B presents the XPS general survey spectrum for the Ni 2p core level of C2 and pure α-$Ni(OH)_2$. The Ni 2p XPS spectrum shows two major peaks centered at around 873.56 and 855.65 eV (Fig. 2B(b)), corresponding to Ni $2p_{1/2}$ and Ni $2p_{3/2}$, respectively, which are characteristic of $Ni(OH)_2$ phases and are in good agreement with previous literature reports.[39,40] Moreover, there are two extra peaks centered at about 879.61 eV and 861.25 eV, which correspond to Ni $2p_{1/2}$ and Ni $2p_{3/2}$ satellites, respectively. For pure α-$Ni(OH)_2$, there are four peaks centered at about 855.62, 861.19, 873.47, and 879.38 eV as shown in Fig. 2B(a). The deconvoluted C (1s) XPS core levels of graphene oxide and C2 are presented in Fig. 2B. We can find a shift to higher energy in the α-$Ni(OH)_2$ TNS/rGO composite compared with that in the single α-$Ni(OH)_2$ sample. This result implies the existence of the interaction and electron transformation between α-$Ni(OH)_2$ and graphene in C2. In our previous work, we also find the interactions between semiconductor oxides and graphene components.[41] The interaction is favorable to improve the activity of semi-conductor oxides. The deconvoluted peak located at the binding energy of 284.9 eV is attributed to the C–C, C═C, and C–H bonds. The deconvoluted peaks centered at the binding energies of 286.8, 287.6, and 289.3 eV are assigned to the C–OH, C═O, and O═C–OH oxygen-containing carbonaceous bands, respectively.[42] This result implies that the chemically exfoliated graphene oxide includes a variety of functional groups such as hydroxyl (C–OH) and epoxide (C–O–C) groups, in addition to carbonyl (–C═O) and carboxyl (–COOH) groups usually present at the defects and edges of the sheets. The XPS analysis of the porous α-$Ni(OH)_2$ TNS/rGO composite (C2) shows a lower percentage area of the C═C peak. This decrease is due to covalently attached α-$Ni(OH)_2$ TNSs that coat the surface of rGO. Also, the XPS of C1s (Fig. 2C(b)) reveals that, compared with GO (Fig. 2C(a)), the oxygenated species is substantially removed with the reduction of GO to graphene.[43]

In addition, the effect of the ratio between Ni and GO is apparent for the formation of dispersed $Ni(OH)_2$ on the rGO. The amount of α-$Ni(OH)_2$ nanosheets assembled on the rGO can be controlled by adjusting the mass ratio of $Ni(NO_3)_2{\cdot}6H_2O$/GO. Fig. 3 shows SEM and TEM images of the composites with different loading amounts of α-$Ni(OH)_2$ on the rGO. As can be seen in Fig. 3a and b, a mass of α-$Ni(OH)_2$ thin nanosheets are clearly visible on the surface and intercalation of the rGO. It is worth noting that when the mass ratio of $Ni(NO_3)_2{\cdot}6H_2O$/GO is 10 : 1 (sample C2, seen in Fig. 1), the α-$Ni(OH)_2$ displays thinner nanosheets and the rGO is thinner. With the increased mass ratio of $Ni(NO_3)_2{\cdot}6H_2O$/GO, the amount of the hexagon α-$Ni(OH)_2$ assembled on the rGO is increased as well (sample C3, seen in Fig. 3c and d). When the mass ratio of $Ni(NO_3)_2{\cdot}6H_2O$/GO was sequentially increased to 25 : 1 (sample C4, seen in Fig. 5e and f), the rGO was extensively covered with the α-$Ni(OH)_2$ nanosheets completely, and the α-$Ni(OH)_2$ nanosheets overlapped and aggregated. These aggregations of α-$Ni(OH)_2$ nanosheets will affect the properties of the sensing composites. Furthermore, as compared with α-$Ni(OH)_2$ nanosheets in the composites (C1–C4), the nanosheets of pure α-$Ni(OH)_2$ (see Fig. S4, ESI†) transform into the nanoplates with mutual stacks. The above results indicate the importance of the amount of Ni precursor for the structure of the composites.

Sensing performances

As we know, the excellent charge transfer capability plays an important role in the prominent electrochemical performance of $Ni(OH)_2$ and rGO. Similarly, for a resistance-type gas sensor, the principle of gas detection is based on the conductance variation of the sensing element, which depends on the gas atmosphere of the sensing material exposed to some gases.

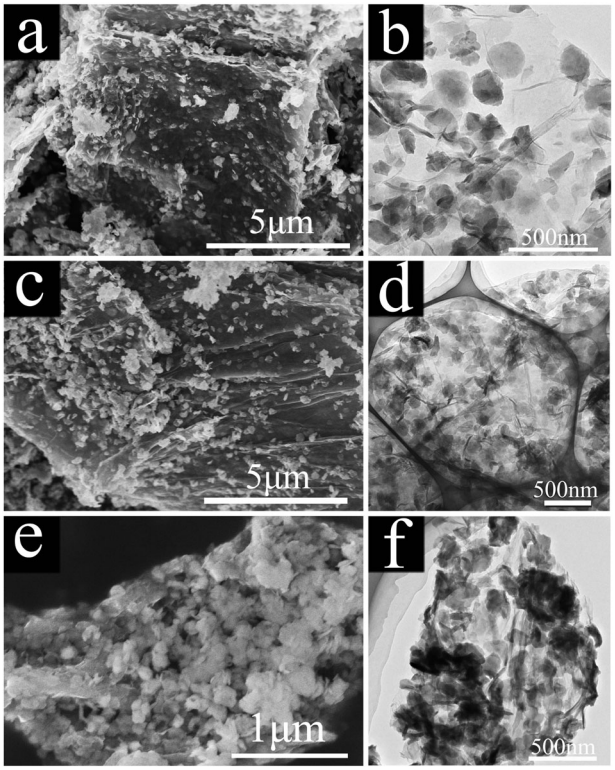

Fig. 3 (a) SEM and (b) TEM images of C1; (c) SEM and (d) TEM images C3; (e) SEM and (f) TEM images of C4.

In our case, the α-$Ni(OH)_2$ TNS/rGO composites might be of great significance as gas sensors. Therefore, we investigated the sensing performance of the samples (C1–C4) to NO_x in air at RT. Fig. 4a and b show the results of gas response of the typical sample C2 sensor in the α-$Ni(OH)_2$/rGO composite thin film sensors during cyclic exposure to decreasing NO_x concentrations from 97 ppm to 0.97 ppm. Fig. 4a displays the typical response–recovery cyclic curves of the sensor with decreasing concentrations of NO_x. When NO gas was injected into the chamber, the resistance of the α-$Ni(OH)_2$ thin film sensor declined rapidly and reached a minimum resistance value in a shorter time. Obviously, the thin-film sensor based on the α-$Ni(OH)_2$ TNS/rGO composite exhibits a rapid and reversible response signal to NO_x gas even at the lowest exposure level (970 ppb), both in adsorption and desorption processes. Fig. 4b shows the corresponding relationship between response and response time under different NO_x concentrations. When the concentration of NO_x is 97.0 ppm, the response time is only 10.0 s, while the highest response reached is 64.4%. It is found that response declined gradually with the decrease in the concentration of NO_x. Also, when the concentration of NO_x was in the range of 97.0–4.85 ppm, the response time was always stable; at a lower NO_x concentration of 2.91 ppm and 970 ppb, the response time increased. Apparently, the response and response time of the sensor are associated with diffused concentration and absorbance of gas on the surface of the nanocomposite.

Furthermore, the gas response of the synthesized α-$Ni(OH)_2$ TNS/rGO composites with varied mass proportions of $Ni(NO_3)_2 \cdot H_2O$/GO to NO_x was also investigated. As can be seen in Fig. 4c, all gas sensors present different degrees of response to NO_x, and the details are listed in Table S1 (ESI†). As expected, the sensor based on sample C2 (10 : 1) exhibited enhanced response for each concentration in the given region compared with that based on other samples. These results strongly prove that the as-prepared α-$Ni(OH)_2$ TNS/rGO nanocomposite with a mass ratio of $Ni(NO_3)_2 \cdot 6H_2O$/GO = 10 : 1 is a promising candidate for gas sensing applications. In addition, the response speeds of the four sensors were rapid, as shown in Fig. 4d and Table S2 (ESI†). By comparison, the response time gradually increases with the decrease in the mass ratio of GO. Namely, the GO in α-$Ni(OH)_2$

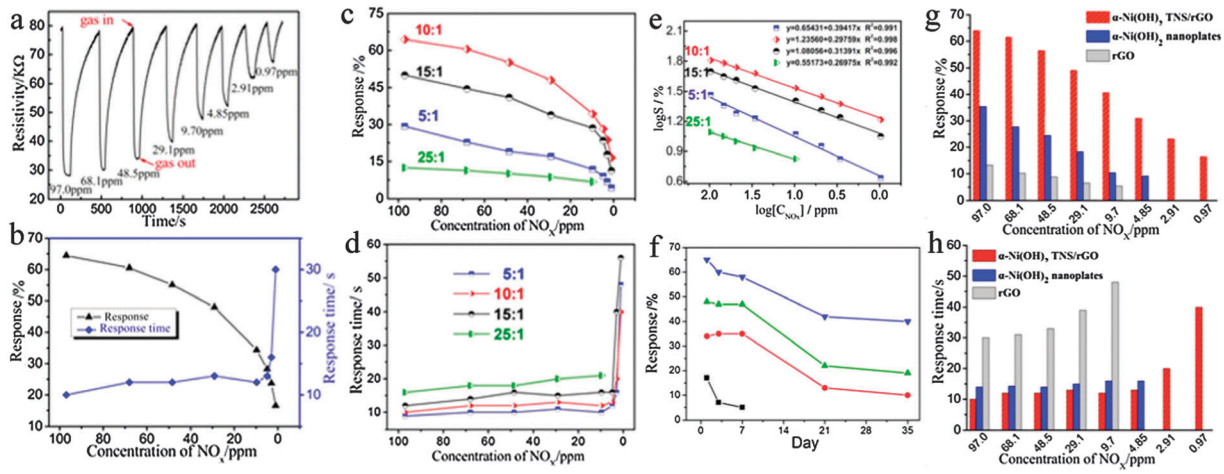

Fig. 4 The results of gas response of α-$Ni(OH)_2$ TNS/rGO composites (a) and (b) the representative response–recovery cyclic curves and corresponding response and response time curve for samples of C2 with concentration of 97–0.97 ppm NO_x in air; (c) and (d) response and response time curves of α-$Ni(OH)_2$ TNS/rGO composites with different mass ratio of $Ni(NO_3)_2 \cdot H_2O$/GO exposed to NO_x with decreasing concentrations; (e) linear dependence relation between the logarithm of response (*S*) and the relative logarithm of NO_x concentration (C) for the C1, C2, C3 and C4 sensor; (f) the stability test of the sensor based on the α-$Ni(OH)_2$ TNS/rGO composite to high and low concentration NO_x; (g) and (h) the bar graphs represent the response and response time of samples for the α-$Ni(OH)_2$ TNs/rGO, α-$Ni(OH)_2$ nanoplates and rGO to NO_x (temperature: 20 °C, humidity: 40%).

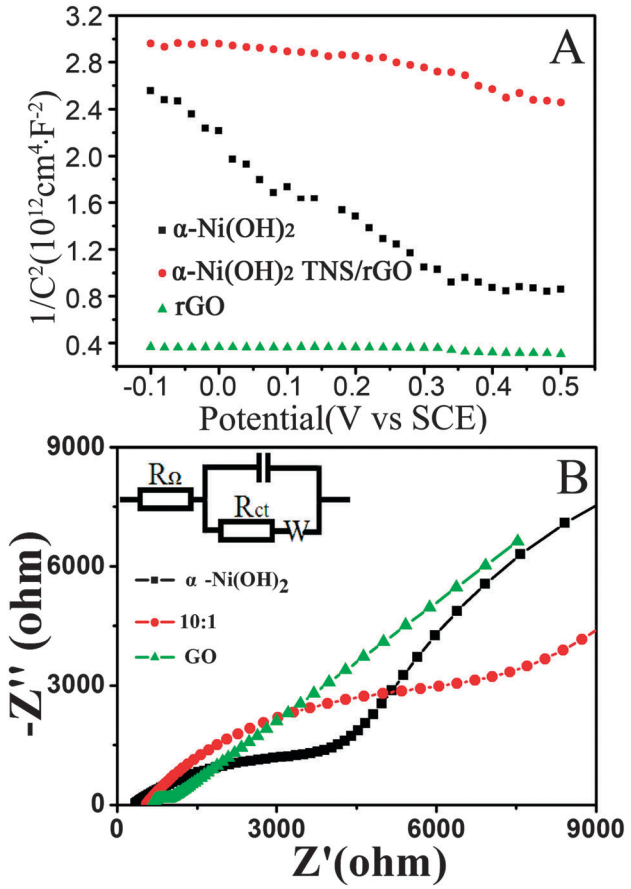

Fig. 5 Mott–Schottky plots of (A) the synthesized samples (α-Ni(OH)$_2$, α-Ni(OH)$_2$ TNS/rGO composite and rGO) electrodes in 3 M KOH solution with a frequency of 10 kHz and (B) Nyquist plots of different and equivalent circuit models of samples (inset) measured in the frequency range from 0.01 Hz to 100 kHz with 0.4 V.

TNS/rGO is critical to response time of the sensor. So, the gas sensor based on sample C2 displays enhanced sensing performance for practical applications since it possesses the highest response and faster response to NO_x.

An interesting phenomenon is found from Fig. 4e, namely, that the sensing response of all α-Ni(OH)$_2$ TNS/rGO composites linearly decreases as a function of NO_x concentrations ranging from 97 ppm to 970 ppb, although the response based on the samples of C1, C3 and C4 is much lower than that based on the sample of C2. From the linear results in Fig. 4e, it can be seen that the response of all α-Ni(OH)$_2$ TNS/rGO composites shows a small rate of decrease, especially the gas sensor based on sample C2, which displays that the value of the linear relationship-R^2-formed by plotting $\log S$ *versus* the $\log[C_{NO_x}]$ is 0.998 (R = 0.999). The result shows that sensors based on α-Ni(OH)$_2$ TNS/rGO composites are available for practical applications in the detection range from 97 ppm to 970 ppb.[44]

The service life of a gas sensor determines its industrial utility, so the stability of the α-Ni(OH)$_2$ TNS/rGO composite-based sensor (sample C2) was investigated as well. Fig. 4f shows the NO_x response of the same sensor at first use and then after being exposed to air at RT for 1, 7, 21 and 35 days. It was found that the response of the sensor did not change significantly over the first three tests. After aging for 35 days and then being exposed to 97 ppm of NO_x, the response of the sensor was 38.9%, which is still higher than that of C1, C3 and C4. The above results indicate that the thin film sensor based on the α-Ni(OH)$_2$ TNS/rGO composite (sample C2) exhibits not only enhanced gas-sensing ability but a longer lifetime response to low-concentration NO_x detection at RT. The longer lifetime response is probably attributed to the novel 3D structure which is constructed with rGO as a substrate and porous α-Ni(OH)$_2$ TNS as blocks. Firstly, the rGO as a substrate of the 3D structure has better stability than any other substrate.[45] Secondly, the three-dimensional structure is more stable than other dimensional sensing materials, such as 0 D nanoparticles, and 2 D fibers, when reacting with target NO_x gas molecules. Beside that, when exposed to air, the three dimensional structure easily recovered. Therefore, the α-Ni(OH)$_2$ TNS/rGO composite have longer lifetime response.

In order to study the selectivity of the C2 sensor, we also measured the response to some gases such as NO_x, NH_3, H_2 and CO at room temperature. As shown in Fig. S5 (ESI†), the C2 sensor exhibits an excellent selectivity for NO_x, and no response to H_2 and CO. Based on the analysis above, the α-Ni(OH)$_2$ TNS/rGO composites obtained *via* simple and green methods used herein could be applied in the gas-sensing field with significant improvements in service life and gas selectivity of sensors for NO_x detection.

Gas sensing mechanism

In order to further discuss the room temperature gas sensing mechanism of α-Ni(OH)$_2$ TNS/rGO, the sensing properties of pure Ni(OH)$_2$, rGO and the C2 sample were studied. The histograms in Fig. 4g and h show the gas-sensing performance of the α-Ni(OH)$_2$ TNS/rGO composite (C2), pure α-Ni(OH)$_2$ nanoplates, and rGO. It can be clearly seen that the gas response of the α-Ni(OH)$_2$ TNS/rGO composite-based sensor to different concentrations of NO_x is considerably better than that of the others. Namely, the α-Ni(OH)$_2$ TNS/rGO composite displays not only higher response to NO_x but also faster response time with the same concentration. Interestingly, the response is decreased in the following order: α-Ni(OH)$_2$ TNS/rGO composites, α-Ni(OH)$_2$ pure α-Ni(OH)$_2$ nanoplates, and rGO, while response time is increased in the order: α-Ni(OH)$_2$ TNS/rGO composites, α-Ni(OH)$_2$ TNS/rGO composites, pure α-Ni(OH)$_2$ nanoplates, and rGO in the detection range. This means that as compared with pure α-Ni(OH)$_2$ nanoplates and rGO, the composites display enhanced gas response. We proposed that the enhancement of the response is due to the synergic effect of Ni(OH)$_2$ and rGO. Therefore, we further study the electrical properties of the three samples.

To the best of our knowledge, the carrier densities of materials play an important role in their gas sensing responses; the appropriate resistance and better electron transportation in air will induce the higher response and faster response. To study the electrical characteristics of α-Ni(OH)$_2$ TNS/rGO composites, MS and EIS measurements were carried out.

The MS analysis using the mono-frequency capacitance–voltage (C–V) sweep is the standard technique to investigate the Schottky contacts in the semiconductor devices. The conduction types of the samples were determined using Mott–Schottky (MS) measurements.[46,47] Fig. 5A shows the MS plots of electrodes based on the synthesized samples. The negative slopes of MS plots for all the samples show a p-type semi-conducting behavior.[48] The carrier density was calculated using the equation $(1/C^2)/V = -2/(q\varepsilon_0\varepsilon_r N_D)$, where $1/C^2$, q, ε_0, ε_r and N_D represent the slope of MS plots, the elementary electric charge (1.60×10^{-19} C), vacuum permittivity (8.85×10^{-14} F cm^{-1}), the relative permittivity of $Ni(OH)_2$ and the carrier density. The carrier densities of α-$Ni(OH)_2$, the α-$Ni(OH)_2$/rGO composites with a mass ratio of 10 : 1, and rGO are 3.90×10^{18}, 1.27×10^{19} and 9.80×10^{19}, respectively. MS studies show that the carrier densities of the α-$Ni(OH)_2$/rGO composite are between that of the pure α-$Ni(OH)_2$ and rGO.

The EIS of sample electrodes were measured to investigate their kinetic processes: the results are shown in Fig. 5B. The electron transportation ability of the samples was studied. The EIS of α-$Ni(OH)_2$, the α-$Ni(OH)_2$/rGO composite (sample C2), and the rGO electrodes were measured to investigate their kinetic processes; the results are shown in Fig. 5B. Here, R_Ω indicates the uncompensated bulk resistance of the electrolyte, the separator and the electrode; R_{ct} is attributed to the charge-transfer resistance at the active material interface; and C is the constant phase angle element, involving double layer capacitance. It can be seen that all of the samples have a small faradic charge transfer resistance. The impedance of the sample electrodes is shown in Table S3 (ESI†). A straight sloping line represents the diffusive resistance of the electrolyte in the electrode pores and the proton diffusion in the host materials. Both R_Ω and R_{ct} are related to the conductivity of the electrodes.[49,50] Furthermore, the values of the resistance R_Ω and charge-transfer resistance R_{ct} are 772 and 3.10×10^3 for C2, respectively, which are close to those of the pristine $Ni(OH)_2$ (579.5 and 2.74×10^3). Therefore, the charge-transfer resistance of the C2 sample nearly shows no change, compared with the pristine $Ni(OH)_2$. Therefore, according to the MS and EIS analysis, the enhancement of the sensing properties appropriate due to the improvement of the carrier densities of the α-$Ni(OH)_2$/rGO composite.

On the basis of the above results, a mechanism has been proposed to understand this change in resistance by using the basic adsorption chemistry on the surface of α-$Ni(OH)_2$ grown on rGO. Many researchers have demonstrated that the adsorption of the NO_x molecule on the graphene surface is *via* weak van der Waals interactions.[51,52] After the reduced graphene oxide surface was decorated by α-$Ni(OH)_2$ TNSs, the sensor response to the NO_x gas is markedly enhanced, and the gas sensing mechanism is different from that of the pure rGO sensor, due to the existence of α-$Ni(OH)_2$ TNSs. Compared with the weak interaction of NO_2 molecules with graphene, it is reasonably concluded that NO_x molecules interact much more intensively with α-$Ni(OH)_2$ TNSs, and the synergistic effect of rGO and α-$Ni(OH)_2$ TNSs plays an important role in sensing performance.

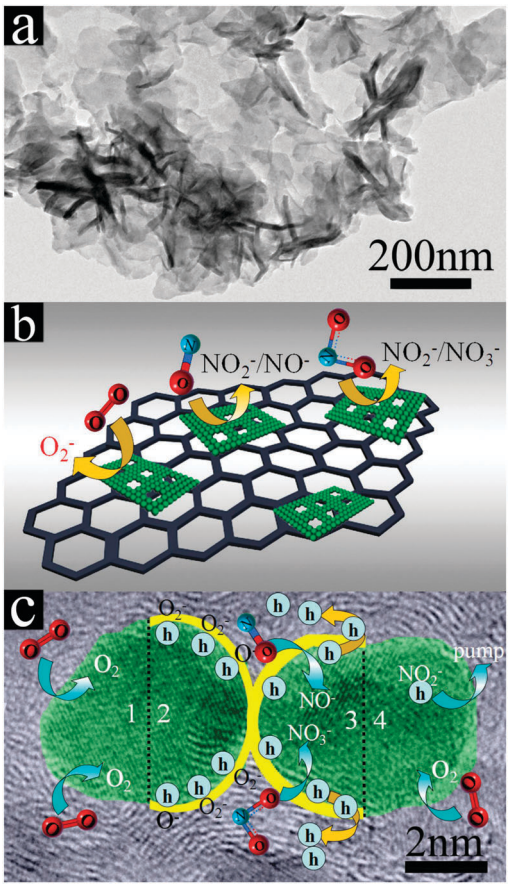

Fig. 6 The scheme of the proposed gas sensing mechanism. (a) The TEM image of the C2; (b) the sketch map of the C2 sensor exposed in NO_x (NO and NO_2); (c) the four NO_x gas sensing successive process on two α-$Ni(OH)_2$ nanoparticles.

We propose that α-$Ni(OH)_2$ TNSs act as a reaction center and catalytically react with detected gas molecules (NO_x) in Fig. 6a. The scheme of the proposed gas sensing mechanism is shown in Fig. 6b and c. The adsorption of NO_2 on the α-$Ni(OH)_2$/rGO composite (sample C2) leads to NO_2^- and the adsorption of NO on C2 leads to NO^- in Fig. 6b. The process traps electrons from the conduction band or the donor level of C2, which finally leads to an increase of hole density. It finally results in a rapid decrease of resistances (see Fig. 4a). The target gas molecules (NO_2) directly adsorb onto C2 and react with O^- and generate bidentate NO_3^-(s). The target gas molecules (NO) also can adsorb onto C2 and react with O^- and generate NO_2^-. Fig. 6c shows the further fine gas sensing mechanism between NO or NO_2 gas molecules and two $Ni(OH)_2$ nanoparticles. Generally, the generation of oxygen adsorbates (O_2^-, O^- or O^{2-}) on the α-$Ni(OH)_2$ surface occurs at high temperatures, and the gas sensing response increases drastically for the metal oxide based gas sensors with particle sizes below the Debye length. In our case, there are four sensing processes as shown in Fig. 6c. First, the oxygen from the air is chemisorbed on the α-$Ni(OH)_2$ surface. Second, the chemisorbed O_2 can react with the electrons near the surface and transform into O_2^- at RT, thus decreasing the concentration of electrons near the surface and

forming a depletion layer. Third, the generated oxygen adsorbent (O_2^-) at the surface of α-Ni(OH)$_2$, when exposed to an oxidizing gas (NO and NO_2), the co-adsorption and mutual interaction between the gases and the adsorbed oxygen result in reduction at the surface and a decrease in the chemisorbed oxygen concentration. The reactions are as follows:

$$NO_2 + e \rightarrow NO^- \quad (1)$$

$$NO_2 + e \rightarrow NO_2^- \quad (2)$$

$$NO + O^- \rightarrow NO_2^- \quad (3)$$

$$NO_2 + O^- \rightarrow NO_3^- \quad (4)$$

Fourth and last, NO and NO_2 were pumped out of the α-Ni(OH)$_2$ TNS/rGO surface, increasing the resistance of C2 to the initial stage, and one cycle of NO_x gas sensing is finished.

Therefore, we think that the enhanced sensing properties of α-Ni(OH)$_2$ TNS/rGO composites are attributed to the synergism of the superior conductivity of the TNS/rGO composites. Compared with that of rGO, the gas molecule contact area of the rGO coated with α-Ni(OH)$_2$ was increased.

According to the literature reported in recent years, a relatively weak and unstable sensing response is the challenge when employing graphene alone for high performance sensing applications. Composites of inorganic materials and graphene with some groups as gas sensing materials have demonstrated good response for the detection of NO_2,[53] H_2[54–56] and H_2S.[57] In our case, the α-Ni(OH)$_2$ TNS growth on rGO plays the role of an active center and transmission channel of the charge carrier to adsorb NO_x molecules with strong electron-withdrawing power. The electron transfer from rGO *via* α-Ni(OH)$_2$ to adsorbed NO_x molecules caused hole enrichment in the p-type composite and consequently decreases its resistance. So, in the same gas environment, the sensing performance was enhanced with increased effective adsorbance of NO_x for the resistance-type gas sensor. This means that the effective load of α-Ni(OH)$_2$ on rGO could affect the response of composites to NO_x. Thus, when the mass ratio of $Ni(NO_3)_2{\cdot}6H_2O$/GO was increased to 10 : 1, the sensor based on the α-Ni(OH)$_2$ TNS/rGO composite demonstrated enhanced sensing. With further growth of α-Ni(OH)$_2$, the response showed a gradual declining trend. It can be explained that the partial aggregation of the α-Ni(OH)$_2$ TNS led to the decrease of active sites and effective load of α-Ni(OH)$_2$ on rGO.

Conclusions

In summary, we have demonstrated a facile reflux method to synthesize α-Ni(OH)$_2$ thin nanosheet/reduced graphene oxide (α-Ni(OH)$_2$ TNS/rGO) composites. The α-Ni(OH)$_2$ TNS/rGO composites display excellent sensing performance toward NO_x such as a low detection limit of 970 ppb, a short response time of 9.0 s, and a relatively high response of 64.4%. The enhanced gas sensing could be ascribed to two factors: (i) a rGO nanosheet substrate with high conductivity could form Schittky contact with the α-Ni(OH)$_2$ thin nanosheet, resulting in the fast capturing and migrating of electrons from the conduction band, and (ii) the pores on the α-Ni(OH)$_2$ thin nanosheet can act as channels for gas diffusion and provide more active sites for the reaction of NO_x with surface-adsorbed oxygen ions. It is also expected that the synthesized composites will find applications in other important fields, such as catalysts, fuel cells and supercapacitors.

Acknowledgements

We gratefully acknowledge the support of this research by the Union Funds of the National Natural Science Foundation of China (No. U1034003), Ministry of Education, the Program for Innovative Research Team; the National Natural Science Foundation of China (No. 51572034), the Natural Science Foundation of Changchun University of Science and Technology (No. XQNJJ-2015-07) and Key Laboratory of Functional Inorganic Material Chemistry, Ministry of Education, the Program for Innovative Research.

Notes and references

1 X. J. Luo, Z. Lou, L. L. Wang, X. J. Zheng and T. Zhang, *New J. Chem.*, 2014, 38–84.
2 Q. J. Yu, C. L. Yu, J. Z. Wang, F. Y. Guo, S. Y. Gao, S. J. Jiao, H. T. Li, X. T. Zhang, X. Z. Wang, H. Gao, H. B. Yang and L. C. Zhao, *RSC Adv.*, 2013, **3**, 16619.
3 L. H. Zu, Y. Qin and J. H. Yang, *J. Mater. Chem. A*, 2015, **3**, 10209.
4 Q. Wang, J. Sun, Q. Wang, D. A. Zhang, L. L. Xing and X. Y. Xue, *J. Mater. Chem. A*, 2015, **3**, 5083.
5 K. Yadav, B. R. Mehta and J. P. Singh, *RSC Adv.*, 2015, **5**, 1581.
6 D. Liu, W. W. Lei, S. Qin, L. T. Hou, Z. W. Liu, Q. L. Cui and Y. Chen, *J. Mater. Chem. A*, 2013, **1**, 5274.
7 L. Erades, D. Grandjean, C. Nayral, K. Soulantica, B. Chaudret, P. Menini, F. Parret and A. Maisonnat, *New J. Chem.*, 2006, **30**, 1026.
8 A. Palacios-Padrós, M. Altomare, A. Tighineanu, R. Kirchgeorg, N. K. Shrestha, I. Díez-Pérez, F. Caballero-Briones, F. Sanz and P. Schmuki, *J. Mater. Chem. A*, 2014, **2**, 915.
9 W. Zhang, J. L. Tian, Y. A. Wang, X. T. Fang, Y. Q. Huang, W. X. Chen, Q. L. Liu and D. Zhang, *J. Mater. Chem. A*, 2014, **2**, 4543.
10 Z. Y. Jin, P. P. Li, G. Y. Liu, B. Z. Zheng, H. Y. Yuan and D. Xiao, *J. Mater. Chem. A*, 2013, **1**, 14736.
11 B. J. Hansen, N. Kouklin, G. Lu, I. K. Lin, J. Chen and X. Zhang, *J. Phys. Chem. C*, 2010, **114**, 2440.
12 S. Park, S. An, H. Ko, C. Jin and C. Lee, *ACS Appl. Mater. Interfaces*, 2012, **4**, 3650.
13 M. Chen, Z. Wang, D. Han, F. Gu and G. Guo, *Sens. Actuators, B*, 2011, **157**, 565.

14 C. Marichy, N. Donato, M. G. Willinger, M. Latino, D. Karpinsky, S. H. Yu, G. Neri and N. Pinna, *Adv. Funct. Mater.*, 2011, **21**, 658.
15 N. D. Hoa and S. A. El-Safty, *Chem. – Eur. J.*, 2011, **17**, 12896.
16 H. Wang, J. Gao, Z. Li, Y. Ge, K. Kan and K. Shi, *CrystEngComm*, 2012, **14**, 6843.
17 Z. Y. Chu, H. X. Sun, H. Xu, J. Zhou, G. Zhang, Y. Xie, L. Li and K. Y. Shi, *RSC Adv.*, 2015, **5**, 101760.
18 J. Liu, H. Bai, Y. Wang, Z. Liu, X. Zhang and D. D. Sun, *Adv. Funct. Mater.*, 2010, **20**, 4175.
19 Y. Qiu, K. Yan, S. Yang, L. Jin, H. Deng and W. Li, *ACS Nano*, 2010, **4**, 6515.
20 Y. Liang, H. Wang, H. S. Casalongue, Z. Chen and H. Dai, *Nano Res.*, 2010, **3**, 701.
21 S. Zhuang, X. Xu, B. Feng, J. Hu, Y. Pang, G. Zhou, L. Tong and Y. Zhou, *ACS Appl. Mater. Interfaces*, 2014, **6**, 613.
22 M. Chen, C. Zhang, L. Li, Y. Liu, X. Li, X. Xu, F. Xia, W. Wang and J. Gao, *ACS Appl. Mater. Interfaces*, 2013, **5**, 13333.
23 H. Huang, Y. Liu, Q. Gao, W. Ruan, X. Lin and X. Li, *ACS Appl. Mater. Interfaces*, 2014, **6**, 10258.
24 J. Song, L. Xu, C. Zhou, R. Xing, Q. Dai, D. Liu and H. Song, *ACS Appl. Mater. Interfaces*, 2013, **5**, 12928.
25 Z. Wang, Y. Xiao, X. Cui, P. Cheng, B. Wang, Y. Gao, X. Li, T. Yang, T. Zhang and G. Lu, *ACS Appl. Mater. Interfaces*, 2014, **6**, 3888.
26 C. Hou, Q. Zhang, M. Zhu, Y. Li and H. Wang, *Carbon*, 2011, **49**, 47.
27 V. Chandra, J. Park, Y. Chun, J. W. Lee, I. C. Hwang and K. S. Kim, *ACS Nano*, 2010, **4**, 3979.
28 F. He, J. Fan, D. Ma, L. Zhang, C. Leung and H. L. Chan, *Carbon*, 2010, **48**, 3139.
29 H. Wang, H. S. Casalongue, Y. Liang and H. Dai, *J. Am. Chem. Soc.*, 2010, **132**, 7472.
30 H. Wang, J. T. Robinson, G. Diankov and H. Dai, *J. Am. Chem. Soc.*, 2010, **132**, 3270.
31 H. G. Na, Y. J. Kwon, H. Y. Cho, S. Y. Kang, T. K. Jung, H.-S. Lee and H. W. Kim, *J. Nanosci. Nanotechnol.*, 2015, **15**, 9002.
32 Y. Yang, C. G. Tian, L. Sun, J. C. Wang, K. Y. Shi, W. Zhou and H. G. Fu, *Nanoscale*, 2014, **6**, 7369.
33 G. Lu, S. Park, K. Yu, R. S. Ruoff, L. E. Ocola, D. Rosenmann and J. Chen, *ACS Nano*, 2011, **2**, 1154.
34 G. Lu, L. E. Ocola and J. Chen, *Nanotechnology*, 2009, **20**, 445502.
35 A. Prakash, S. Chandra and D. Bahadur, *Carbon*, 2012, **50**, 4209.
36 Y. Ren and L. Gao, *J. Am. Ceram. Soc.*, 2010, **93**, 3560.
37 M. Cao, X. He, J. Chen and C. Hu, *Cryst. Growth Des.*, 2007, **7**, 170.
38 P. Jeevanandam, Y. Koltypin and A. Gedanken, *Nano Lett.*, 2001, **1**, 263.
39 D. P. Dubal, G. S. Gund, C. D. Lokhande and R. Holze, *ACS Appl. Mater. Interfaces*, 2013, **5**, 2446.
40 G. Wang, Y. Ling, X. Lu, T. Zhai, F. Qian, Y. Tong and Y. Li, *Nanoscale*, 2013, **5**, 4129.
41 B. Jiang, C. Tian, Q. Pan, Z. Jiang, J. Q. Wang, W. Yan and H. Fu, *J. Phys. Chem. C*, 2011, **115**, 23718.
42 O. Akhavan, *ACS Nano*, 2010, **4**, 4174.
43 C. Xu, X. Wang and J. Zhu, *J. Phys. Chem. C*, 2008, **112**, 19841.
44 R. J. Wu, J. G. Wu, T. K. Tsai and C. T. Yeh, *Sens. Actuators, B*, 2006, **120**, 104.
45 H. J. Yoon, D. H. Jun, J. H. Yang, Z. X. Zhou, S. S. Yang and M. M.-C. Cheng, *Sens. Actuators, B*, 2011, **157**, 310.
46 S. X. Wu, Z. Y. Yin, Q. Y. He, G. X. Lu, Z. Zhou and H. Zhang, *J. Mater. Chem.*, 2011, **21**, 3467.
47 M. C. McShane and K. S. Choi, *J. Am. Chem. Soc.*, 2009, **131**, 2561.
48 H. Y. Wu, K. Kan, L. L. Wang, G. Zhang, Y. Yang, H. Li, L. Q. Jing, P. K. Shen, L. Li and K. Y. Shi, *CrystEngComm*, 2014, **16**, 9116.
49 D. D. Cai, P. C. Lian, X. F. Zhu, S. Liang, W. Yang and H. Wang, *Electrochim. Acta*, 2012, **74**, 65.
50 D. H. Xia, S. Z. Song and J. H. Wang, *Trans. Nonferrous Met. Soc. China*, 2012, **22**, 717.
51 R. K. Joshi, H. Gomez, F. Alvi and A. Kumar, *J. Phys. Chem. C*, 2010, **114**, 6610.
52 J. D. Fowler, M. J. Allen, V. C. Tung, Y. Yang, R. B. Kaner and B. H. Weiller, *ACS Nano*, 2009, **3**, 301.
53 H. Y. Jeong, D. S. Lee, H. K. Choi, D. H. Lee, J. E. Kim, Y. L. Jeong, W. J. Lee, S. O. Kim and S. Y. Choi, *Appl. Phys. Lett.*, 2010, **96**, 213105.
54 U. Lange, T. Hirsch, V. M. Mirsky and O. S. Wolfbeis, *Electrochim. Acta*, 2011, **56**, 3707.
55 R. Kumar, D. Varandani, B. R. Mehta, V. N. Singh, Z. Wen, X. Feng and K. Müllen, *Nanotechnology*, 2011, **22**, 275719.
56 J. L. J ohnson, A. Behnam, S. J. Pearton and A. Ural, *Adv. Mater.*, 2010, **22**, 4877.
57 T. V. Cuong, V. H. Pham, J. S. Chung, E. W. Shin, D. H. Yoo, S. H. Hahn, G. H. Rue, E. J. Kim, S. H. Huh and P. A Kohl, *Mater. Lett.*, 2010, **64**, 2479.